

Assessment of interface deformation and fracture in metal matrix composites under transverse loading conditions

THEODORE E. MATIKAS*

Department of Materials Science and Engineering, University of Ioannina, University Campus, 45110 Ioannina, Greece

Received 19 February 2008; accepted 3 March 2008

Abstract—The transverse properties of unidirectional metal matrix composites (MMCs) are dominated by the fiber/matrix interfacial properties, residual stresses and matrix mechanical response. In order to monitor and study, *in situ*, the failure of interfaces in titanium-based composites subjected to transverse loading conditions, an ultrasonic imaging technique has been developed. The interface was imaged ultrasonically and the change in ultrasonic amplitude with the transverse loading was monitored, indicating the sensitivity of the technique to fracture and deformation of interfaces. This change in amplitude has been explained in terms of the multiple reflection theory of ultrasonic waves. The multiple reflection theory enabled estimation of the interfacial deformation and debonding as a function of loading. The ultrasonic technique was also used in conjunction with finite element modeling in order to quantify the fiber/matrix interfacial transverse strength *in situ* in MMCs.

Keywords: Metal matrix composites; interface elastic property; transverse loading; interfacial fracture; ultrasonic nondestructive evaluation.

1. INTRODUCTION

Metal matrix composites, reinforced with continuous silicon carbide (SiC) fibers, offer superior properties along the fiber axis. However, this gain is at the expense of properties in the transverse direction [1–4]. It is clear that the transverse properties of MMCs are dominated by the interfacial properties, residual thermal stresses and matrix mechanical response [5–18]. Nimmer *et al.* [7, 8], using both modeling and experimental approaches, have shown that the ‘knee’ in the transverse stress–strain curves of Ti-6Al-4V/SiC composites is associated with a perfectly weak bond interface and residual thermal stresses. The work by Wisnom [9, 10] has indicated that the transverse strength and strain to failure of 6061 aluminum/SiC composites depend strongly on the bond strength of the fiber/matrix interface. Other

*E-mail: matikas@otenet.gr

studies [18] also suggest that interfacial crack initiation and propagation in titanium-based composites are related to the bond strength of the interfacial region. The interfacial region (i.e. interface coating or reaction product) between the fiber and matrix is known to exist in most metal matrix composites. Since the load transfer between the fiber and matrix depends on the properties and conditions of this interfacial region, the mechanical behavior of the composites is strongly affected by its characteristics. More recent studies [19–21] clearly indicate the important role the interface plays in transverse properties of MMCs. Therefore, it is essential to assess the fracture behavior and deformation of the interfaces in MMCs in order to contribute to understanding of the dependence of the composite's transverse properties on the interfacial properties.

In this paper, the failure of the fiber/matrix interfaces under transverse loading conditions has been investigated, *in situ*, utilizing an ultrasonic imaging technique called shear back reflectivity technique (SBR) developed by Matikas and Karpur [22–25]. The SBR technique was found to be more sensitive to the interfacial conditions than traditional ultrasonic imaging techniques using longitudinal waves [22] and was used to evaluate the fiber/matrix interface elastic property, matrix texture, consolidation quality, high temperature degradation of MMCs and fiber fracture in matrices [22–27]. The current study applies this technique to the investigation of interfacial fracture and deformation of titanium-based composites under transverse loading conditions.

2. EXPERIMENTAL

2.1. Materials and mechanical testing

Monofilament Ti-6Al-4V composite samples were used in this study containing a single SiC (SCS-6) fiber. The purpose of using the single-fiber composites was to avoid fiber interactions that occur in high volume fiber-reinforced composites. Thus, the intrinsic phenomena related to the interfacial fracture and deformation could be studied with clarity, thereby providing 'building blocks' for the analysis of high volume fiber-reinforced composites. The composites were fabricated by hot pressing two Ti-6Al-4V sheets with a single SiC fiber in between at 930°C with 17 MPa pressure for 2 h. To prevent damage to the fiber's surface during the consolidation process, the single fiber was aligned before hot pressing by placing it in a fiber retention groove in one of the titanium sheets. The groove had the depth of the fiber diameter (140 µm) and was introduced through a specially-constructed shaping apparatus. Assuring good consolidation is essential for obtaining meaningful results on interface fracture strength under transverse loading conditions. Figure 1 shows a well-consolidated Ti-6Al-4V/SCS-6 sample. The consolidated samples were cut into dog-bone shape with the fiber axis perpendicular to the loading axis of the samples. Transverse tensile tests were carried out using a micro-straining stage. The loading was applied stepwise (interrupted loading) so that the ultrasonic scanning

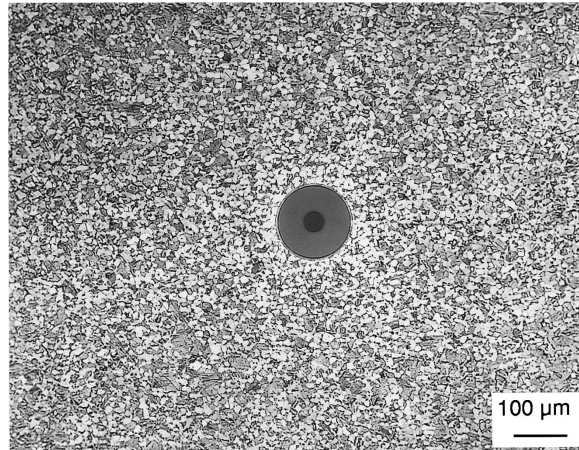


Figure 1. Metallography of a monofilament Ti-6Al-4V/SCS-6 composite showing good consolidation.

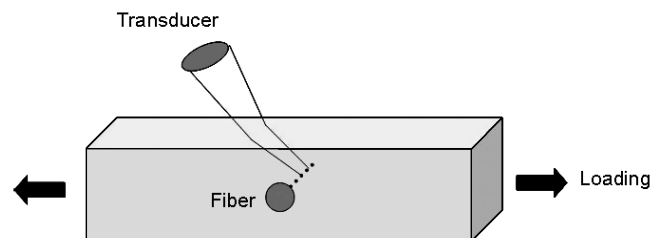


Figure 2. Experimental setup for ultrasonic monitoring of transverse loading test.

could be carried out under loading condition at different stress levels (Fig. 2). For each ultrasonic scanning, optical micrographs of edge replicas of the composites were taken to benchmark ultrasonic observation with microscopic damage of the fiber/matrix interface during transverse loading.

2.2. Ultrasonic imaging

The experimental setup for ultrasonic imaging using the SBR technique is shown in Fig. 3. The transversely-loaded composite specimen was immersed in water and imaged in a pulse-echo mode with an ultrasonic beam incident angle $\theta_I = 24^\circ$, which is between the first critical angle (i.e. the incident angle at which compressional ultrasonic waves cease to propagate in the material, which is 13.8° for Ti-6Al-4V) and the second critical angle (i.e. the incident angle at which shear waves also cease to propagate in the material, which is 28.4° for Ti-6Al-4V). As a result, only vertically polarized ultrasonic shear waves were propagated in the matrix material, and were incident on the fiber/matrix interface perpendicular to the axis of the fiber, as shown in Fig. 3. The direction of propagation of shear waves in Ti-6Al-4V was at an angle $\theta_S = 62^\circ$ with respect to the normal to the water/sample interface, as predicted by the Snell's law, $c_w/\sin(\theta_I) = c_S/\sin(\theta_S)$, where $c_w = 1440$ m/s and $c_S = 3120$ m/s

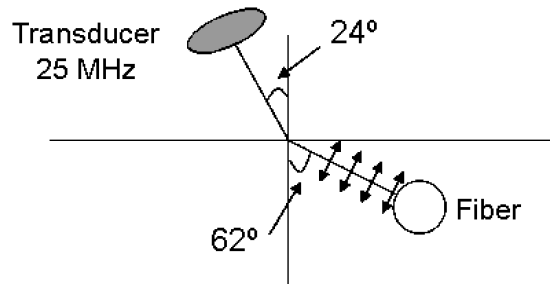


Figure 3. Experimental setup of ultrasonic SBR imaging technique. The transmitted shear wave in the matrix material at 62° with respect to the normal of the water/Ti-6Al-4V interface is based on the Snell's law of refraction.

are the sound velocity in water and Ti-6Al-4V, respectively. The back-received ultrasonic signal in this case was either of low amplitude, due to back-scattering from matrix grains, or of high amplitude, due to the back-reflection from the fiber/matrix interface where the wave front was perpendicular to the fiber circumference. This ultrasonic amplitude, varying along the fiber, produced the ultrasonic image of the interface. A 25 MHz focused ultrasonic transducer was used to produce C-scan images of the interface [28]. The ultrasonic beam had a focal area with diameter approximately $140\ \mu\text{m}$, which was of the order of the SiC fiber's diameter.

2.3. Finite element analysis

Finite element analysis (FEA) of the single-fiber composites was implemented for Ti-6Al-4V/SCS-6 sample as an example to explain some of the ultrasonic experimental results using the ANSYS code [29]. The fiber and matrix were described using three-dimensional eight-node isoparametric elements, while the interfacial region was treated as a thin layer with a finite thickness and independent properties, and was simulated using three-dimensional eight-node concrete solids. The concrete solids can crack if the specified fracture strength of the solids is exceeded [18, 29]. After a crack is initiated, no singularity at the crack tip has been treated in this study. Instead, the crack tip stresses are averaged over the entire element next to the crack, leading to a size dependence of the stresses on the element next to the crack. Therefore, the prediction for the crack initiation stress is rigorous in this study, while the prediction for the crack propagation stress should be taken with reservation.

The SiC fiber considered was assumed to be isotropic and homogeneous with temperature-independent, linear elastic properties: $E = 414\ \text{GPa}$, $\nu = 0.3$ and $\alpha = 4.86 \times 10^{-6}/^\circ\text{C}$ ($T_{\text{ref}} = 900^\circ\text{C}$) [7, 8]. The titanium matrix (Ti-6Al-4V) was also assumed to be isotropic, homogeneous and have the following elastoplastic properties:

$$\begin{aligned}\sigma_e &= 113\,800 \times \varepsilon \text{ (MPa),} && \text{for elastic regime,} \\ \sigma_p &= 881 + 2085 \times \varepsilon \text{ (MPa),} && \text{for plastic regime,}\end{aligned}$$

where ε is the true strain, and σ_e and σ_p are the true stresses at the stage of elastic and plastic deformation, respectively. These properties of the matrix at room temperature were measured in this study from the neat materials which had gone through the same processing cycle as the composite specimens. The matrix was further assumed to obey the von Mises yield criterion with an isotropic work hardening capability, and having $\nu = 0.3$ and $\alpha = 9.8 \times 10^{-6}/^\circ\text{C}$ ($T_{\text{ref}} = 900^\circ\text{C}$) [30]. The interfacial region (i.e. the graded carbon–silicon coating) was assumed to be very weak with fracture strength of 5 MPa. This assumption was based on the work conducted by Nimmer *et al.* [7, 8] who have shown that the interface between Ti-6Al-4V and SCS-6 SiC fiber is very weak due to the presence of the graded carbon–silicon coating. The other properties of the coating were assumed: $\nu = 0.3$, $E = 100$ GPa and $\alpha = 4.86 \times 10^{-6}/^\circ\text{C}$. Here, the elastic modulus and coefficient of thermal expansion (CTE) of the coating were taken to be within the upper ($E = 800$ GPa, $\alpha \simeq 9 \times 10^{-6}/^\circ\text{C}$) and lower ($E = 10$ GPa, $\alpha \simeq -1 \times 10^{-6}/^\circ\text{C}$) bounds of C/C composites [31, 32] because of the difficulty of measuring the *in situ* properties of the coating.

The finite element mesh used in this work is shown in Fig. 4. Three types of elements were utilized: (a) matrix elements with plasticity using the von Mises criterion coupled with an isotropic work hardening assumption; (b) fiber elements that exhibit an elastic behavior; and (c) interfacial elements capable of cracking in tension and crushing in compression with independent thermal and mechanical properties. The fiber diameter was set to be 140 μm corresponding to the typical diameter of SCS-6 SiC fibers. The composite was assumed to be infinite in the direction of fiber axis (i.e. the z -coordinate direction). In the y -direction, the composite was assumed to have a thickness of 2 mm corresponding to the actual thickness of the test specimens. In the direction perpendicular to the fiber axis (i.e.

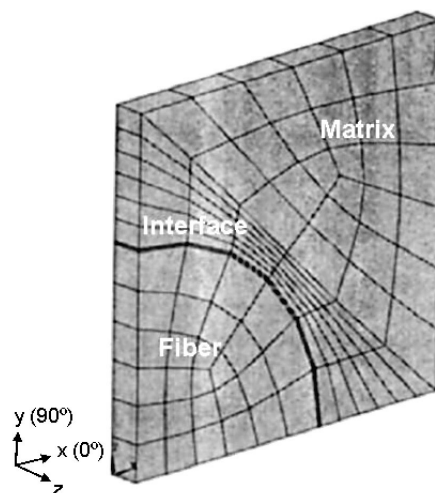


Figure 4. Finite element mesh used to model single-fiber composites. The transverse load is applied along the x -axis.

the x -direction), a length of 4 mm was assumed. This is believed to be sufficient for the simulation of the test specimens because, at the distance of about three times the fiber diameter away from the fiber, the stresses in the matrix are almost uniform [33]. The interface was assumed to have a thickness of 1 μm to stand for the graded carbon–silicon coating on the SCS-6 fiber. The 1 μm thickness was chosen arbitrarily because it has been demonstrated [18] that the interfacial crack initiation and propagation are not affected by the thickness of the coating when the coating is within typical thickness range (0.5 to 3.0 μm). The boundary conditions in this study were set in such a way that one-eighth of the composite could be used to represent the behavior of the whole composite. Specifically, the nodes on the bottom face of the model (i.e. the x – z plane at $y = 0$) were not allowed to move in the y -direction, while the nodes on the top face of the model were free to move. The nodes on the y – z plane at $x = 0$ were not allowed to move in the x -direction, while the nodes on the y – z plane at $x = 2$ were coupled together to move the same distance in the x -direction. Similarly, the nodes on the back face of the model (i.e. the x – y plane at $z = 0$) were not allowed to move in the z -direction, while the nodes on the front face of the model were coupled in the z -direction.

Both thermal and transverse mechanical loads were considered in this study. The composites were assumed to be quenched from 800°C to 25°C. The zero stress state of the composites was assumed to be at 800°C and the thermal loads were applied under the assumption that the temperature is spatially uniform throughout the composites. After the cooling event, the mechanical load was superimposed to the residual thermal stresses by applying a transverse stress in the x -direction.

3. RESULTS

3.1. Ultrasonic imaging

A typical stress–strain curve for the transverse tensile test and the corresponding ultrasonic shear wave images at different levels of stresses are shown in Fig. 5. The letters ‘A–J’ in Fig. 5 correspond to various stress levels as labeled in the stress–strain curve. Image ‘A’ shows the fiber before any applied load. Images ‘B’ to ‘E’ show the fiber subjected to transverse loading at stress levels from 50 MPa to 300 MPa, where no interface fracture was observed. Drop in the amplitude of the signal was observed in image ‘F’ (at about 450 MPa). The embedded in the matrix reflector (damaged interface) had no cylindrical form when the entire interface was fractured; therefore, the reflected signal from the fractured interface did not reach the maximum value. Images ‘G’ (680 MPa) through ‘J’ (930 MPa) illustrate the physical separation between matrix and fiber. The area of physical separation does not have the same slope along the length of the fiber. Therefore, the back-reflected amplitude significantly varies along the fiber’s length. After the complete release of applied load, a significant drop of the back-reflected amplitude was observed (image ‘K’). This is due to change in the residual stresses at the interface.

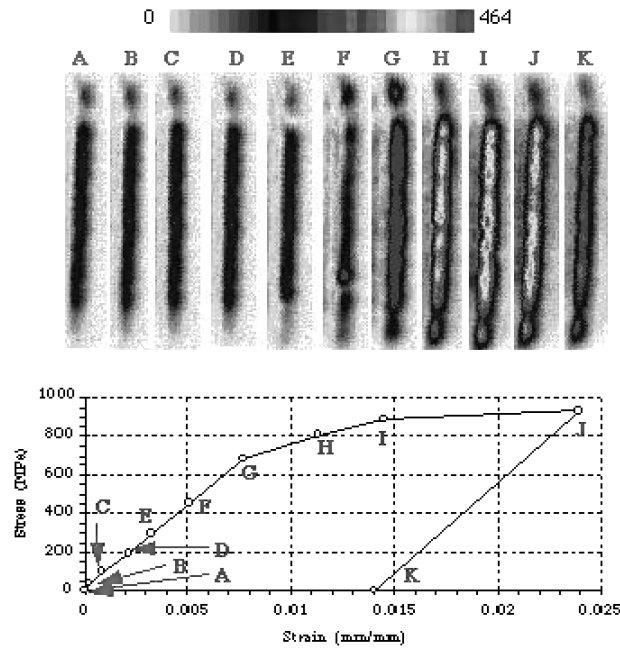


Figure 5. *In situ* ultrasonic SBR imaging of a single-fiber composite during various stages of transverse loading.

Several salient features can be observed in the above mentioned images. First, the back-reflected ultrasonic amplitude does not exhibit a monotonic increase with increasing stress level. Second, the amplitude along the fiber axis varies with position. Third, high amplitude locations at zero loads generally remain at high amplitude as compared to the other locations. Finally, image separation occurs at the two ends of the fiber. This phenomenon is due to the stress reversal at the free surface (i.e. the region where the fiber intersects a free surface) and has been discussed elsewhere [34] in detail. The phenomena displayed in Fig. 5 held true for all the three specimens tested in the present study.

3.2. Microscopic damage at the interface

The edge replicas of the same composite shown in Fig. 5 are presented in Fig. 6. Figure 6 depicts the evolution of the microscopic damage in a Ti-6Al-4V composite with a single SiC fiber. Based on the stress levels, it can be seen that Fig. 6(a–e) correspond to the image of A, E, F, G and J in Fig. 5, respectively. The far-field loading axis is perpendicular to the fiber and vertical in Fig. 6. Note that different magnifications are used in Fig. 6 to maintain focus as much as possible on both the matrix and fiber. This is necessary because of fiber protrusion under high stress loading. The fiber protrusion after the interfacial failure is driven by the release of the axial compressive stresses in the fiber and is enhanced by the contraction of the matrix due to the Poisson's effect and volume conservation during

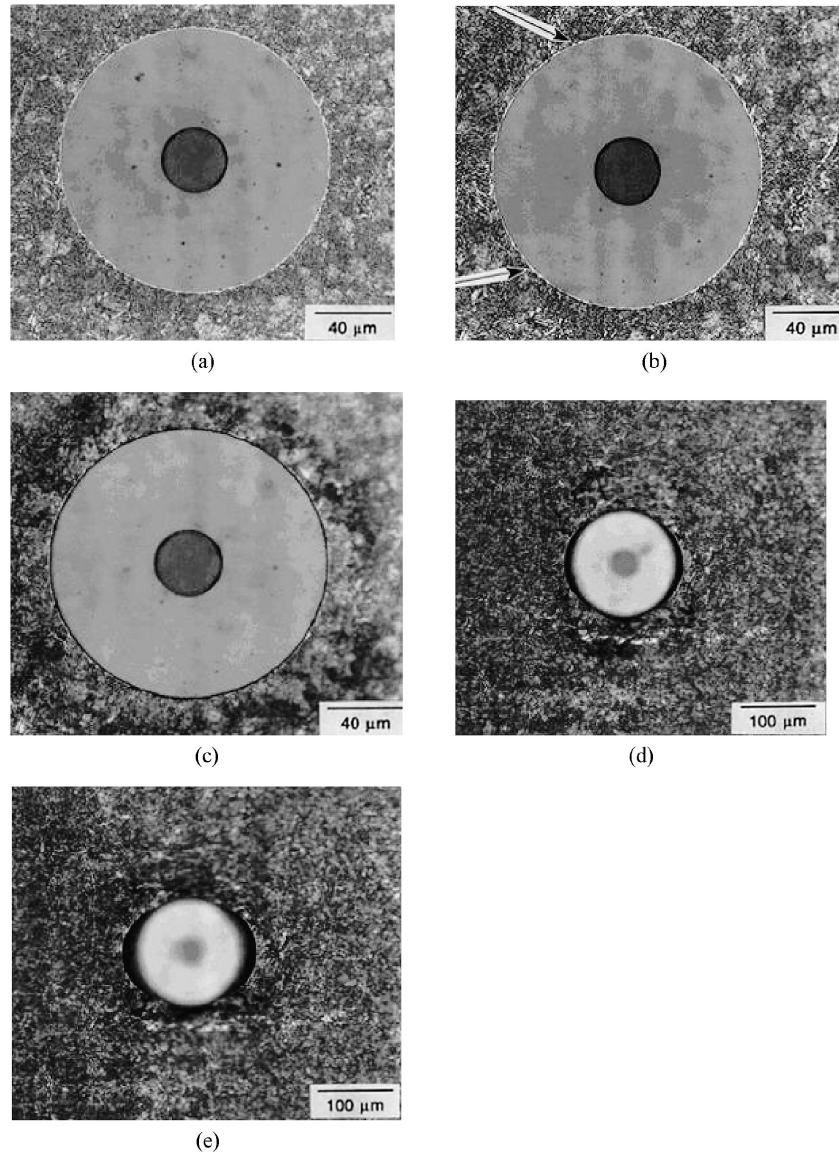


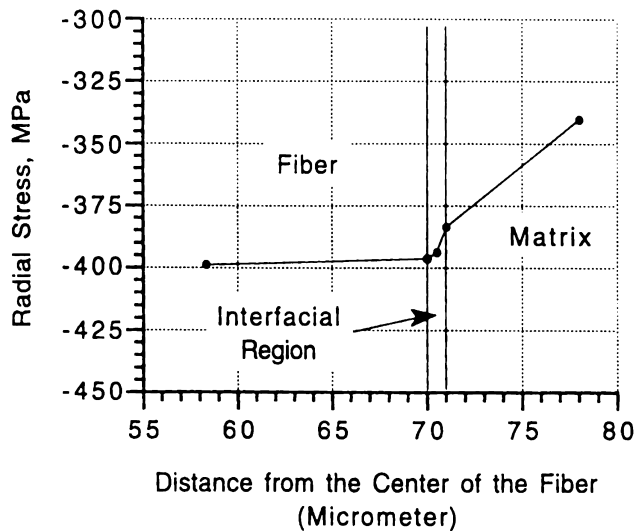
Figure 6. Optical micrographs of the edge replicas of the same composite sample shown in Fig. 5 taken at various loading conditions: (a) as received (zero load) — corresponding to image ‘A’ in Fig. 5. The fiber/matrix interface appears to be intact after small amount of load has been applied thereby decreasing the radial compressive residual stress at the interface. (b) 300 MPa — corresponding to image ‘E’ in Fig. 5. As the load increases in the elastic range the interface chemical bond fails on the sides of the fiber (between the two arrows) in the direction of loading. (c) 450 MPa — corresponding to image ‘F’ in Fig. 5. As the load further increases in the elastic range, the chemical bonding of the entire interface fails. (d) 680 MPa — corresponding to image ‘G’ in Fig. 5. As the load increases even more in the elastic range, physical separation between the matrix and the fiber takes place. (e) 930 MPa — corresponding to image ‘J’ in Fig. 5. In the plastic range, the physical separation between the matrix and the fiber becomes more and more pronounced.

elastic and plastic deformation. It is clear that interfacial debonding has occurred at or below the far-field stress of 300 MPa, as evidenced by the dark fringe along the circumference of the fiber (Fig. 6(b)) which does not exist before the loading (Fig. 6(a)). Furthermore, the interface at near 0° with respect to the loading axis has opened up to some extent at a stress 300 MPa, as indicated by the formation of ridges of acetate in Fig. 6(b). The ridges formed at this stress level are very small, suggesting the commencement of interfacial separation at about 300 MPa. As the loading increases, the acetate ridges become longer and thicker, manifesting the spread-out of the interfacial separation towards the location at 90° with respect to the loading axis. At 930 MPa (Fig. 6(e)) the matrix around the fiber has plastically deformed so much that it appears as elliptical. At the same time, the fiber protrusion under this stress is $9\ \mu\text{m}$ above the matrix and the length of the acetate ridges is about $30\ \mu\text{m}$. As such, the fiber and acetate ridges are both out of focus in the optical micrograph.

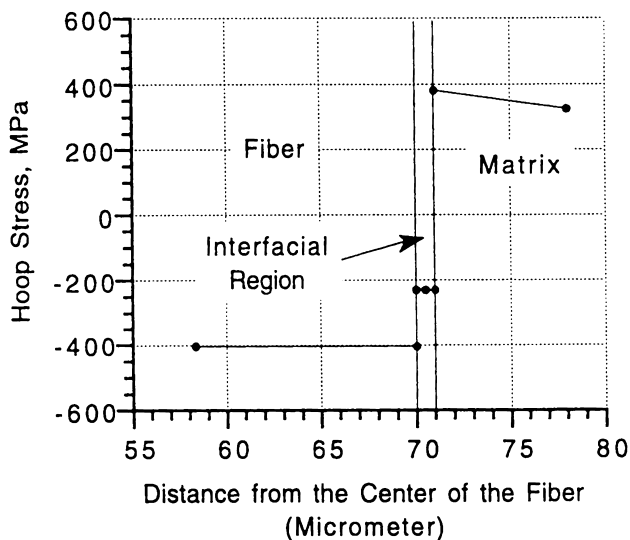
3.3. Stress analysis and failure of the interface from FEA

The residual radial and hoop stresses induced during the cool down from 800°C to 25°C near the interfacial region are shown in Fig. 7. As expected, the larger CTE of the matrix as compared to the fiber and interfacial region creates a tensile hoop stress and a compressive radial stress in the matrix, while the fiber and interfacial region are in compression for both the hoop and radial stresses. The compressive radial stresses at the interface provide clamping stresses against the interfacial debonding. Thus, the interfacial region cracks only after the clamping stresses have been overcome. The modeling shows that when the far-field stress reaches 270 MPa, the x -stress at the interfacial region of about 45° with respect to the loading axis (the x -axis in Fig. 4) has exceeded the fracture strength of the interfacial region (which is 5 MPa). As such, a crack (interfacial debonding) initiates at that location and propagates along the interfacial region instantly towards 0° . However, the interfacial region from $\sim 50^\circ$ to 90° is still intact because of the presence of the residual compressive stresses. Only up to about 360 MPa far-field stress, does the crack propagate along the whole circumference of the interface. Above this stress level, the load is carried by the matrix alone. The flow field and interfacial separation between the fiber and matrix as a function of the stress can also be obtained from the current modeling. Since the strongest back-reflected signals come from the interfaces located at about 30° with respect to the tensile axis (Fig. 3), the interfacial separation at the location of 30° as a function of the far-field loading is presented in Fig. 8. It can be seen that after the crack initiation at 270 MPa, the matrix and fiber at the 30° start to separate gradually as the loading increases. The increase in the separation becomes fast above 800 MPa because of the plastic deformation of the matrix.

It is interesting to mention that the single-fiber composite has a larger compressive radial stress and a smaller tensile hoop stress as compared to 30 vol% SiC composites with the same cool down conditions [18]. As a result, cracking at the



(a)



(b)

Figure 7. Residual thermal stresses near the interfacial region induced during the cool down from 800°C to 25°C: (a) radial and (b) hoop stresses.

interface occurs at a higher stress level (270 MPa) for the single-fiber composite than that (160 MPa) for the 30 vol% SiC composites. Finally, it should be pointed out that the current modeling is only for the interior of the composite because of the assumption of the infinite length of the composite in the fiber axis, thereby neglecting the effect of the free surface. If the effect of free surface is considered, then at the cool down conditions of MMCs there is a tensile radial residual thermal stress at the interfacial region, extending from the free surface (where the residual

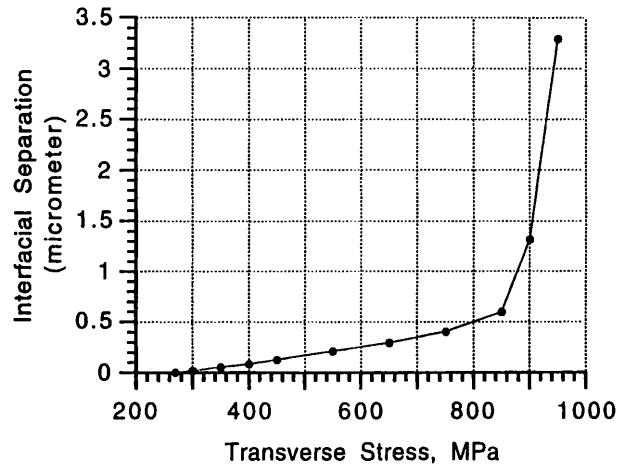


Figure 8. Interfacial separation between matrix and fiber at the location of 30° with respect to the tensile axis as a function of the far-field stress.

stress is maximum) to the inner side up to a distance of about 0.15 times the fiber diameter ($0.15d = 20 \mu\text{m}$) at which it becomes zero [34]. With the presence of tensile radial stress, interfacial cracking near the free surface occurs at a much lower stress level than the value required for the same failure to commence at the interior of the composite [35, 36]. After the distance of $\sim 20 \mu\text{m}$, the radial residual stress at the interface becomes compressive, progressively increasing up to the distance of about $2d = 280 \mu\text{m}$, at which it becomes constant [34]. After this distance the effect of free edge ceases to exist. Based on the consideration of radial residual stresses, the extent of interfacial debonding is predicted different between the free surface and inner side. The maximum crack opening displacement, approximately $0.04 \mu\text{m}$, is found at the free edge.

4. DISCUSSION

Detailed examination of Fig. 5 indicates that the amplitude of the ultrasonic image varies with the far-field stress as follows. First, it stays more or less constant at the early stage of loading. Then, it decreases as the far-field stress reaches about 300 MPa. This is followed by a sharp increase in the amplitude as the stress exceeds 700 MPa. Finally, the amplitude decreases again after large plastic deformation. The stress dependence of the ultrasonic amplitude may be related to several mechanisms. First, the amplitude relies on the acoustic impedance mismatch between the two media. The coefficient of reflection, R , is related to the acoustic impedance, Z , by [37]:

$$R = \frac{Z_2 - Z_1}{Z_2 + Z_1} = \frac{\sqrt{\rho_2 \mu_2} - \sqrt{\rho_1 \mu_1}}{\sqrt{\rho_2 \mu_2} + \sqrt{\rho_1 \mu_1}} = \frac{\rho_2 C_2 - \rho_1 C_1}{\rho_2 C_2 + \rho_1 C_1}, \quad (1)$$

where ρ , μ and C are the density, shear modulus and shear wave velocity, respectively. The subscripts 1 and 2 refer to the two media, with 1 being the medium where the incident wave propagates and 2 the medium where the transmitted wave propagates. Before the interfacial debonding, medium 1 is the titanium matrix and medium 2 is the fiber. After the debonding occurs, medium 2 becomes water since the specimen is immersed in water. Therefore, an amplitude change in the reflected wave is expected due to the debonding. Other mechanisms which may change the amplitude include residual thermal stresses in the media [38, 39], elastic and plastic deformation of the media [40–42], the fiber diameter [22], the angle of incidence [22], the frequency of the ultrasonic wave used [22] and the microstructural details at the interface. Various investigations [35, 39] have revealed that shear wave velocity depends on the residual stresses in the medium. Such dependency has been attributed to a change in density as well as a change in the relevant elastic constants of the medium under stresses. However, the change of the velocity is found to be below 1% [38–40]. Similarly, elastic and plastic deformation of the medium induced by statically applied stresses alters the shear wave velocity to a very limited extent (less than 1% variation) [40–42]. As such, it is expected that the stress change in the composite specimens during the loading has very limited influence on the coefficient of reflection owing to the small changes in density and shear wave velocity (see equation (1)). The fiber diameter, the frequency of the ultrasonic wave, and the angle of incidence at the water/matrix interface are constant in the present study. However, due to the plastic deformation of the matrix under high stress loading (Fig. 6(e)), the angle of incidence at the matrix/water interface (inside the composite) at a specified spatial location varies with loading. Even with this variation of the incident angle, no change in the amplitude of the reflected wave is expected because C-scan is conducted and a position at which the incident wave is normal to the matrix/water interface always exists. As such, the incident wave can be regarded to be always normal to the fiber/matrix interface or matrix/water interface. Therefore, it can be concluded that any significant changes in the amplitude of the reflected wave are associated with the evolution of damage at the fiber/matrix interface.

The evolution of interfacial damage during the transverse loading test is illustrated in Fig. 9. During the initial stages of loading, the radial compressive residual stresses at the interface are decreasing while the interfacial chemical bond remains intact. As the load further increases (in the elastic range) partial failure of the chemical bond occurs, starting from the two opposite sides of the fiber in the direction of loading and progressing to entire interfacial debonding. During this stage, no observable physical separation exists between the matrix and the fiber. As the load continues to increase (still in the elastic range) physical separation occurs between matrix and fiber in the direction of loading. This separation progressively increases with the raise of load in the plastic range and a change of slope of the damaged area is observed (pronounced elliptical form around the interface).

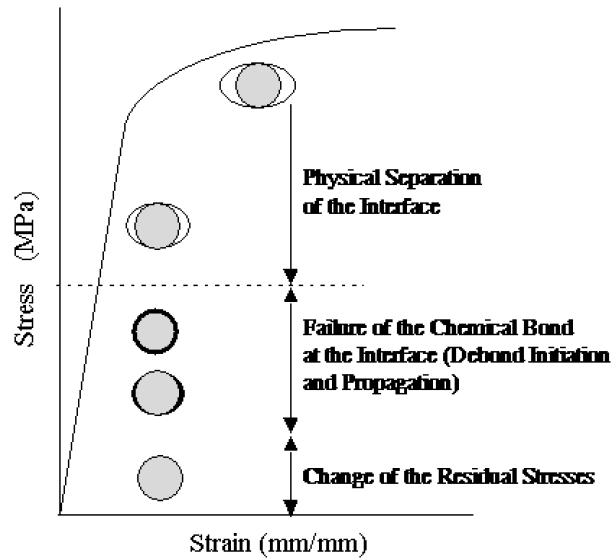


Figure 9. Evolution of interfacial damage during transverse loading of a composite sample.

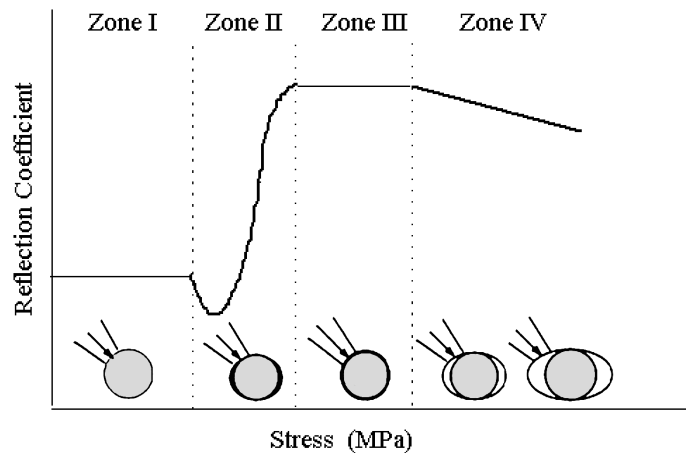


Figure 10. Schematic of the relationship between interfacial damage and ultrasonic back-reflection coefficient using the SBR technique.

Figure 10 depicts the predicted back-reflected ultrasonic amplitude as a function of interfacial damage during the transverse loading test. During the initial steps of the transverse test an ultrasonic beam is incident on an intact interface (zone I). In this case, the embedded in the matrix reflector is a perfect cylinder (i.e. a well-consolidated cylindrical fiber) and the amplitude of the back-reflected ultrasonic signal can be predicted by the theoretical model [22] for the specific composite system. As the failure of interface chemical bonding begins, part of the ultrasonic beam would be incident on the bonded fiber and the other part of the beam would be incident on the fractured interface, causing destructive interference between the

positive and negative reflections of the two parts of the beam, resulting in reduced total back-reflected amplitude (zone II). It should be pointed out that this drop in amplitude may not always be observed because it depends on the load increment interruption chosen for ultrasonic imaging. As the failure of interfacial chemical bonding progresses and complete interfacial fracture is achieved, the back-reflected amplitude reaches a maximum value (zone III), as predicted by the theoretical model [22] and experimental verification using simulated debonding [23]. Finally, as the load further increases and physical separation occurs and progresses, the back-reflected ultrasonic amplitude slightly drops, due to the fact that the embedded reflector is not cylindrical any longer; therefore, part of the incident wave is reflected away from the receiver causing the amplitude to drop in value (zone IV). While the physical separation between matrix and fiber continues to grow it is possible that the slope of the opening crack surface becomes perpendicular to the axis of the incident ultrasonic beam. In such case, the back-reflected amplitude would further increase then would start decreasing again with further change in the slope of damaged area.

Predicted changes of the back-reflected ultrasonic amplitude as a function of interfacial damage evolution can be explained in terms of the multiple reflection theory of ultrasonic waves. Examination of Fig. 6(a–e) reveals that the interfacial region in Ti-6Al-4V/SCS-6 SiC composites consists of two interfaces: Ti-6Al-4V/graded carbon–silicon coating/SiC. For brevity in writing, the graded carbon–silicon coating will be called the carbon coating in the text that follows. Under transverse loading, debonding typically occurs inside the carbon coating at the interface of carbon sublayers, at the carbon/Ti-6Al-4V interface and/or at the carbon/SiC interface. To simplify the problem, only the debonding at the carbon/SiC interface is assumed for the present discussion. As such, after the debonding there, three interfaces now exist: Ti-6Al-4V/carbon, carbon/water and water/SiC interfaces. Therefore, the back-reflected signals before the debonding are the results of reflection from two interfaces, while the signals after the debonding are the results of reflection from three interfaces. Multiple reflection of a wave from plane layers has been treated in details by Brekhovskikh [43]. In his work, a general case has been considered: there are $n + 1$ media, and the wave coming from the $(n + 1)$ th medium reaches the first layer consisting of medium n and is split into a transmitted and a reflected wave. After passing through the first layer, the transmitted wave is split again at the second interface (i.e. the interface between the n th medium and the $(n - 1)$ th medium) and so on. Based on the boundary conditions in the transition through the interfaces, he has arrived at an equation describing the reflection coefficient from n interfaces:

$$R = \frac{Z_{\text{in}}^{(n)} - Z_{n+1}}{Z_{\text{in}}^{(n)} + Z_{n+1}}, \quad (2)$$

where Z_{n+1} and $Z_{\text{in}}^{(n)}$ are the acoustic impedance of the $(n + 1)$ th medium and the input impedance of the entire set of the other media (i.e. the n layers below

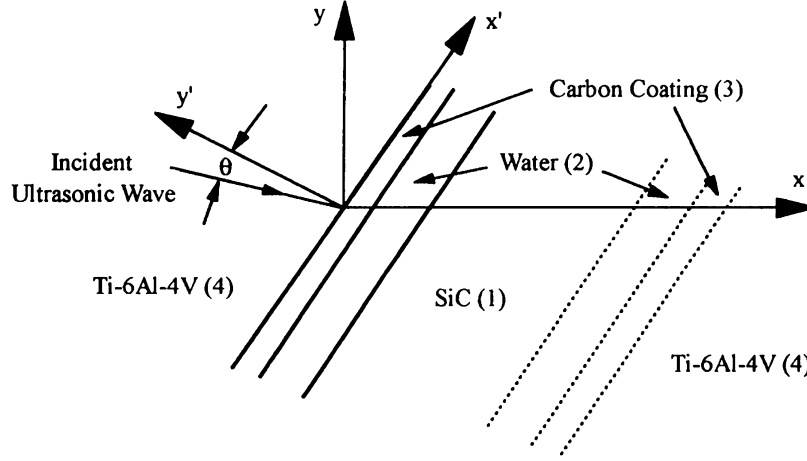


Figure 11. A simplified four-medium system for modeling multiple ultrasonic reflection in Ti-6Al-4V/SCS-6 composites.

the $(n + 1)$ th medium), respectively. The input impedance is determined from the formula

$$Z_{\text{in}}^{(n)} = Z_n \frac{Z_{\text{in}}^{(n-1)} - i Z_n \tan(k_{ny'} d_n)}{Z_n - i Z_{\text{in}}^{(n-1)} \tan(k_{ny'} d_n)}, \quad (3)$$

where Z_n and $Z_{\text{in}}^{(n-1)}$ are the acoustic impedance of the n th medium and the input impedance of the entire set of the $(n - 1)$ layers below the n th medium, respectively; d_n is the thickness of the n th medium; and $k_{ny'}$ is the component of the wave vector along the direction normal to the interface in the n th medium. $Z_{\text{in}}^{(n-1)}$ is in turn determined by making the substitution of $Z_{\text{in}}^{(n-1)}$ for $Z_{\text{in}}^{(n)}$ on the left side of equation (3) and $Z_{\text{in}}^{(n-2)}$ for $Z_{\text{in}}^{(n-1)}$, Z_{n-1} for Z_n , $k_{(n-1)y'}$ for $k_{ny'}$, and d_{n-1} for d_n on the right side of the equation. The rest of the input impedances, $Z_{\text{in}}^{(n-2)}$ and so on, can be found by following the aforementioned substitution rules.

For our current situation, the reflection can be simplified as a four medium system, as shown in Fig. 11. Without loss of generality, all the curved interfaces have been replaced by plane interfaces because the strongest back-reflected signals come from the interfaces located at about 30° with respect to the tensile axis (Fig. 2). Furthermore, the titanium matrix and the SiC fiber have been assumed to be infinite. Although a more detailed modeling with symmetrical interfaces with respect to the SiC plate can be conducted (dashed lines in Fig. 11), the above assumption has simplified the calculation and is a good approximation to the composite. Corresponding to this simplified model, equations (2) and (3) can be re-written as

$$R = \frac{Z_{\text{in}}^{(3)} - Z_4}{Z_{\text{in}}^{(3)} + Z_4}, \quad (4)$$

with

$$\begin{aligned}
 Z_{\text{in}}^{(3)} = & Z_3 (Z_1 Z_2 - Z_1 Z_3 \tan(k_{2y'} d_2) \tan(k_{3y'} d_3) \\
 & - i [Z_2^2 \tan(k_{2y'} d_2) + Z_2 Z_3 \tan(k_{3y'} d_3)]) \\
 & \times (Z_2 Z_3 - Z_2^2 \tan(k_{2y'} d_2) \tan(k_{3y'} d_3) \\
 & - i [Z_1 Z_2 \tan(k_{2y'} d_2) + Z_2 Z_1 \tan(k_{3y'} d_3)])^{-1}. \quad (5)
 \end{aligned}$$

The subscripts 1, 2, 3 and 4 refer to SiC, water, carbon coating, and Ti-6Al-4V, respectively, as shown in Fig. 11. Reflection before the debonding corresponds to a special case of $d_2 = 0$. The input data for the current composite system are summarized in Table 1. As mentioned in Section 2.3, the *in situ* properties of the carbon coating are difficult to measure. Therefore, it is assumed that the elastic modulus of the coating is within the upper (800 GPa) and lower (10 GPa) bounds of the observed elastic moduli for C/C composites [31, 32]. The thickness of the coating is assumed to be 2 μm , corresponding to the thickness of the coating. The incident angle, θ , at the fiber/matrix interface (Fig. 11) is assumed to be so small (from -5 to 5°) that $k_{ny'}$ ($k_{ny'} = k_n \cos \theta$) is taken to be equal to the wave vector, k_n , in the modeling. Acoustic impedance of shear wave is used for all the solids, while acoustic impedance of longitudinal wave is used for water. The results from the modeling are presented in Fig. 12 which shows the back-reflection coefficient, R , as a function of the interfacial separation (i.e. the thickness of the water layer). Because of the trigonometric functions in equation (5), R fluctuates regularly between fixed limits with increasing water thickness. The period for the present four medium systems is 14.4 μm , a number equal to one quarter of the wave length of the ultrasound traveling in the water. As a result, reflection reaches its first maximum amplitude at the interfacial separation of 7.2 μm . It should be pointed out that the period obtained is precisely half of that for three medium systems with water as the thickness-changing layer [37]. Details of R as a function of the interfacial separation are shown in Fig. 12(b). Before debonding R equals 0.1825, which starts to decrease as the debonding occurs. At about 0.13 μm of separation, R reaches its

Table 1.

Parameters of the Ti-6Al-4V/SCS-6 composite system related to ultrasonic testing

Material	Elastic modulus (GPa)	Shear modulus (GPa)	Density (g/cm^3)	Longitudinal bar velocity (m/s)	Shear wave velocity (cm/s)	Acoustic impedance (N s m^{-3})
Ti-6Al-4V [24]	113.8	43.04	4.43	5070	3120	2.246×10^7 (L) 1.381×10^7 (S)
Water			1.0	1440		1.44×10^6 (L)
SCS-6 [6]	414.0	155.25	3.2	1137	6960	3.638×10^7 (L) 2.227×10^7 (S)
Carbon [25, 26]	100.0	37.50	2.25	6670	4080	1.500×10^7 (L) 9.185×10^6 (S)

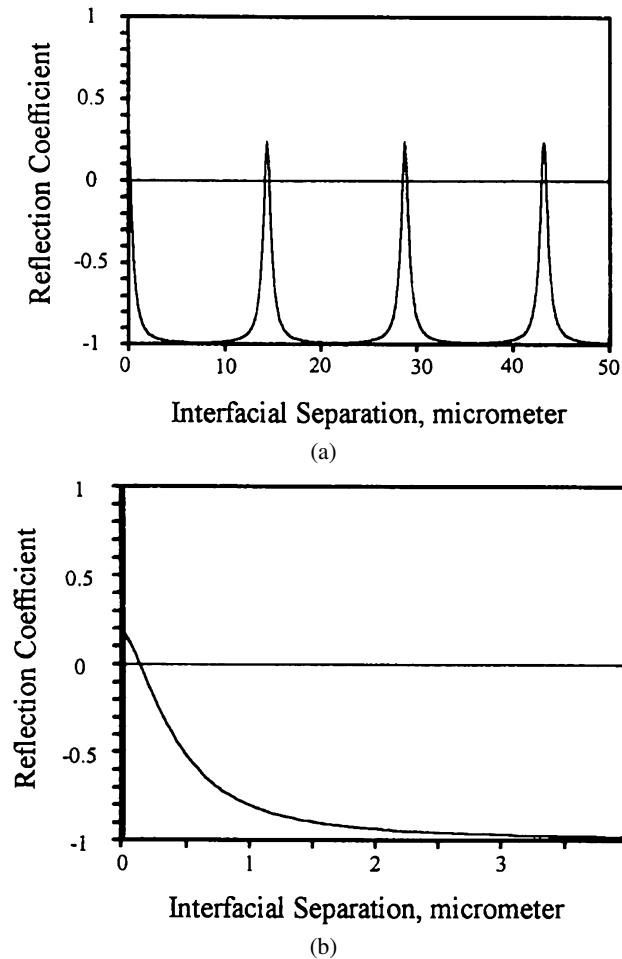


Figure 12. (a) Reflection coefficient as a function of the interfacial separation calculated from the four-medium system shown in Fig. 11 and (b) portion of the curve for small interfacial separation.

lowest value. As the separation continues to increase, R starts to increase but with a 180° phase shift. This increase in R continues until the separation reaches $7.2 \mu\text{m}$ (shown in Fig. 12(a)). Combined with the finite element analysis on the interfacial separation (Fig. 8), R as a function of the far-field stress can be found and is shown in Fig. 13. Included in Fig. 13 are also the R values before the interfacial debonding for which no stress effects have been taken into account. Furthermore, the absolute value of R is presented to exhibit the magnitude of the reflected wave. It can be seen that the model predicts: (1) R stays more or less constant at the early stage of loading; (2) R starts to decrease as the far-field stress reaches about 300 MPa; and (3) after passing the minimum at about 450 MPa, R starts to increase and becomes obviously larger than the reflection coefficient before the loading, as the stress exceeds 650 MPa. Clearly, the prediction, depicted in Fig. 10, shows the same

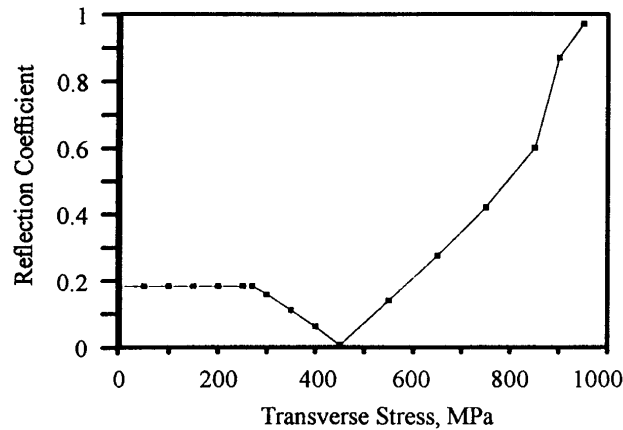


Figure 13. Reflection coefficient as a function of transverse stress, calculated by combining multiple reflection theory of ultrasonic waves and finite element modeling.

trend as the experimental observation except the observed decrease in the amplitude of the back-reflected wave after large plastic deformation. The discrepancy at the large plastic deformation is likely due to the plane interface assumption and/or the simplification of the infinite SiC plate.

The trend observed in the experiments is also supported by the replica observations. At about 100 MPa, sliding of the fiber occurs only at the free surface region due to the residual tensile radial stresses at the free surface. However, the depth of debonding along the fiber-axis-direction is small at this stress level. Thus, the ultrasonic image does not change with the occurrence of the sliding because of the long wave length of the ultrasound used (about 120 μm in the Ti-6Al-4V matrix). At about 300 MPa, the interfacial separation starts, as evidenced by replica technique (Fig. 6). Although the separation is observed on the free surface, it is an indicator of the deformation in the interior of the composite. One related study [44] using automated deformation mapping technique has shown that the flow field of the matrix at the x - y plane (Fig. 4) and the interfacial separation in the interior of the composite are similar to those observed on the composite surface under transverse loading. Therefore, the replica data suggest that the interface in the interior of the composite debonds at or below 300 MPa. As such, the back-reflected signal becomes weaker corresponding to the onset of the interfacial debonding. The increase in thickness of the acetate ridges with increasing loading suggests the increase in the interfacial separation with increasing loading, leading to the decrease at first and then the increase in the amplitude as the loading increases.

Finally, it should be pointed out that the non-uniform amplitude of the back-reflected wave in Fig. 5 is likely due to a non-uniform interfacial microstructure, as shown in Fig. 6. The non-uniformity of the interface is caused by the different reaction tendencies of α and β phases in the Ti-6Al-4V with the coating [45, 46]. The non-uniformity of the interface is on the scale of grain size (about 10 μm), comparable to the wave length in Ti-6Al-4V (about 120 μm). Thus, the scattering

is considerably different along the interface, leading to the non-uniform amplitude of the back-reflected wave. This non-uniformity in the interfacial microstructure persists even after the debonding. Therefore, high amplitude locations generally remain high amplitude at different stresses, as compared to the other locations.

5. CONCLUSION

The present study has utilized an ultrasonic imaging technique, the Ultrasonic Shear Wave Back Reflectivity technique, to *in situ* monitor and study the failure of the fiber/matrix interface of titanium-based composites subjected to transverse loading conditions. The ultrasonic imaging, coupled with replica metallography and finite element analysis, has been proven to be sensitive to the fracture and deformation of the interfaces in Ti-based MMCs. The change in the amplitude of the ultrasonic images with transverse loading can be summarized as follows: (1) the amplitude stays more or less constant at the early stage of the loading; (2) it starts to decrease, corresponding to the commencement of the interfacial debonding; and (3) as the loading continues to increase, the amplitude decreases at first and then increases sharply, corresponding to a monotonic increase in the interfacial separation. The stress dependency of the ultrasonic images can be explained in terms of the theory of multiple reflection of a wave from plane layers. Based on the multiple reflection theory, the interfacial separation as a function of the loading can be estimated from the ultrasonic images. Due to the sensitivity of this imaging technique to interfacial debonding, the technique can be used to quantify the interfacial strength *in situ*, if the technique is combined with finite element modeling, and therefore can be applied to study the dependency of the composite transverse properties on the fiber/matrix interface.

REFERENCES

1. J. M. Larson, W. C. Revelos and M. L. Gambone, An overview of potential titanium aluminide composites in aerospace applications, in: *Intermetallic Matrix Composites II, MRS Proc.*, D. B. Miracle, D. L. Anton and J. A. Graves (Eds), Vol. 273, pp. 3–16. Materials Research Society, Pittsburgh, PA, USA (1992).
2. T. W. Chou, A. Kelly and A. Okura, Fibre-reinforced metal-matrix composites, *Composites* **16**, 187–206 (1985).
3. N. Carrere, R. Valle and T. Bretheau, Multiscale analysis of the transverse properties of Ti-based matrix composites reinforced by SiC fibres: from the grain scale to the macroscopic scale, *Intl J. Plasticity* **20**, 783–810 (2004).
4. O.-H. Kwon and J.-W. Kang, The stress analysis and the crack behavior according to the characteristic of the interfacial region in fiber-reinforced MMC, *Intl J. Modern Phys. B* **20**, 4457–4462 (2006).
5. P. E. Chen and J. M. Lin, Transverse properties of fibrous composites, *Mater. Res. Standards* **9**, 29–33 (1969).
6. S. R. Gunawardena, S. Jansson and F. A. Leckie, Modeling of anisotropic behavior of weakly bonded fiber-reinforced MMC's, *Acta Metall. Mater.* **41**, 3147–3156 (1993).

7. R. P. Nimmer, Fiber–matrix interface effects in the presence of thermally induced residual stresses, *J. Compos. Technol. Res.* **12**, 65–75 (1990).
8. R. P. Nimmer, R. J. Bankert, E. S. Russell, G. A. Smith and P. K. Wright, Micromechanical modeling of fiber/matrix interface effects in transversely loaded SiC/Ti-6-4 metal matrix composites, *J. Compos. Technol. Res.* **13**, 3–13 (1991).
9. M. R. Wisnom, Factors affecting the transverse tensile strength of unidirectional continuous silicon carbide fibre reinforced 6061 aluminum, *J. Compos. Mater.* **24**, 707–726 (1990).
10. M. R. Wisnom, Micromechanical modelling of the transverse tensile ductility of unidirectional silicon carbide/6061 aluminum, *J. Compos. Technol. Res.* **14**, 61–69 (1992).
11. D. D. Robertson and S. Mall, Fiber–matrix interphase effects upon transverse behavior in metal–matrix composites, *J. Compos. Technol. Res.* **14**, 3–11 (1992).
12. B. S. Majumdar, G. M. Newaz and J. R. Ellis, Evolution of damage and plasticity in titanium-based, fiber-reinforced composites, *Metall. Trans.* **24A**, 1597–1609 (1993).
13. D. B. Marshall, W. L. Morris, B. N. Cox, J. Graves, J. R. Porter, D. Kouris and R. K. Everett, Transverse strengths and failure mechanisms in Ti₃Al matrix composites, *Acta Metall. Mater.* **42**, 2657–2673 (1994).
14. W. S. Johnson, S. J. Lubowinski and A. L. Highsmith, Mechanical characterization of unnotched SCS-6/Ti-15-3 metal matrix composites at room temperature, in: *Thermal and Mechanical Behavior of Metal Matrix and Ceramic Matrix Composites*, ASTM STP 1080, J. M. Kennedy, H. H. Moeller and W. S. Johnson (Eds), pp. 193–218. American Society for Testing and Materials, Philadelphia, USA (1990).
15. P. K. Wright, N. Nimmer, G. Smith, M. Sensmeier and M. Brun, The influence of the interface on mechanical behavior of Ti-6Al-4V/SCS-6 composites, in: *Interfaces in Metal-Ceramics Composites*, R. Y. Lin, R. J. Arsenault, G. P. Martins and S. G. Fishman (Eds), pp. 559–581. The Minerals, Metals and Materials Society (1989).
16. S. Jansson, H. E. Deve and A. G. Evans, The anisotropic mechanical properties of a Ti matrix composite reinforced with SiC fibers, *Metall. Trans.* **22A**, 2975–2984 (1991).
17. T. W. Clyne and A. J. Philllips, Interfacial control and macroscopic failure in long-fiber-reinforced and laminated inorganic composites, *Compos. Sci. Technol.* **51**, 271–282 (1994).
18. L. Shaw and D. Miracle, Effects of an interfacial region on the transverse behavior of metal–matrix composites, *Acta Metall. Mater.* **44**, 2043–2055 (1996).
19. L. L. Shaw, T. E. Matikas, P. Karpur, S. Hu and D. B. Miracle, Fracture strength and damage progression of the fiber/matrix interfaces in titanium-based MMCs with different interfacial layers, *Composites Part B: Engng* **29**, 331–339 (1998).
20. J. M. Hausmann, S. Emura and C. Leyens, Cyclic behavior of transverse loaded titanium matrix composites, Materials Science and Technology Meeting (2003).
21. N. Carrere, S. Kruch, A. Vassel and J.-L. Chaboche, Damage mechanisms in unidirectional SiC/Ti composites under transverse creep loading: experiments and modelling, *Intl J. Damage Mech.* **11**, 41–63 (2002).
22. T. E. Matikas and P. Karpur, Ultrasonic reflectivity technique for the characterization of fiber–matrix interface in metal matrix composites, *J. Appl. Phys.* **74**, 228–236 (1993).
23. T. E. Matikas and P. Karpur, Micro-mechanics approach to characterize interfaces in metal and ceramic matrix composites, in: *Review of Progress in Quantitative Nondestructive Evaluation*, D. O. Thompson and D. E. Chimenti (Eds), Vol. 13B, pp. 1477–1484. Plenum Press, New York, NY (1994).
24. T. E. Matikas and P. Karpur, Matrix–fiber interface characterization in metal matrix composites using ultrasonic shear-wave back-reflection coefficient technique, in: *Review of Progress in Quantitative Nondestructive Evaluation*, D. O. Thompson and D. E. Chimenti (Eds), Vol. 12B, pp. 1515–1522. Plenum Press, New York, NY (1992).
25. P. Karpur, T. E. Matikas, S. Krishnamurthy and N. Ashbaugh, Ultrasound for fiber fragmentation size determination to characterize load transfer behavior of matrix–fiber interface in metal matrix

- composites, in: *Review of Progress in Quantitative Nondestructive Evaluation*, D. O. Thompson and D. E. Chimenti (Eds), Vol. 12B, pp. 1507–1513. Plenum Press, New York, NY (1992).
26. P. Karpur, D. A. Stubbs, T. E. Matikas, M. P. Blodgett and S. Krishnamurthy, Ultrasonic nondestructive characterization methods for the development and life prediction of titanium matrix composites, in: *Characterization of Fiber Reinforced Titanium Matrix Composites*, AGARD Report 796, 13.1–13.12 (1993).
 27. P. Karpur, T. E. Matikas and S. Krishnamurthy, Ultrasound as a tool for the development of aerospace structural titanium and ceramic matrix composites, in: *Proc. TMS Annual Meeting*, R. Y. Lin and S. G. Fishmans (Eds), pp. 241–253. The Minerals, Metals and Materials Society, San Francisco, California, USA (1994).
 28. T. E. Matikas, M. Rousseau and P. Gatignol, Theoretical analysis for the reflection of a focused ultrasonic beam from a fluid–solid interface, *J. Acoust. Soc. Amer.* **93**, 1407–1416 (1993).
 29. *ANSYS User's Manual*, Swanson Analysis Systems, Inc., Houston, USA PA, I–IV (1992).
 30. *Titanium Alloys Handbook*, Metals and Ceramics Information Center, Battelle Columbus Labs and Air Force Materials Lab, USA, Wright Patterson AFB (1972).
 31. G. Ziegler and W. Huttner, Engineering properties of carbon–carbon and ceramic–ceramic composites, in: *Engineered Materials Handbook — Ceramics and Glasses*, S. J. Schneider (Ed.), Vol. 4, pp. 835–844. ASM International (1991).
 32. M. S. Dresselhaus, G. Dresselhaus, K. Sugihara, I. L. Spain and H. A. Goldberg, *Graphite Fibers and Filaments*. Springer-Verlag, Berlin and Heidelberg, Germany (1988).
 33. D. F. Adams and D. R. Doner, Transverse normal loading of a unidirectional composite, *J. Compos. Mater.* **1**, 152–164 (1967).
 34. S. Hu, P. Karpur, T. E. Matikas, L. Shaw and N. J. Pagano, Free edge effect on residual stresses and debond of a composite fibre/matrix interface, *Mech. Compos. Mater. Struct.* **2**, 215–225 (1995).
 35. N. J. Pagano, Axisymmetric micromechanical stress fields in composites, in: *Local Mechanics Concepts for Composite Material Systems*, J. N. Reddy and K. L. Reifsnider (Eds), pp. 1–26. Springer-Verlag, New York, NY (1991).
 36. E. S. Folias, On the prediction of failure at a fiber/matrix interface in a composite subjected to a transverse tensile load, *J. Compos. Mater.* **25**, 869–886 (1991).
 37. J. Krautkramer and H. Krautkramer, *Ultrasonic Testing of Materials*, 3rd edn. Springer-Verlag, Berlin and Heidelberg, Germany (1983).
 38. J. Noronha and J. J. Wert, An ultrasonic technique for the measurement of residual stress, *J. Test. Eval.* **3**, 147–152 (1975).
 39. D. I. Crecraft, The measurement of applied and residual stresses in metals using ultrasonic waves, *J. Sound Vibr.* **5**, 173–192 (1967).
 40. R. H. Bergman and R. A. Shahbender, Effect of statically applied stresses on the velocity of propagation of ultrasonic waves, *J. Appl. Phys.* **29**, 1736–1738 (1958).
 41. R. T. Smith, Stress-induced anisotropy in solids — the acoustic–elastic effect, *Ultrasonics* **1**, 135–147 (1963).
 42. D. M. Egle and D. E. Bray, Measurement of acoustoelastic and third-order elastic constants for rail steel, *J. Acoust. Soc. Amer.* **60**, 741–744 (1976).
 43. L. M. Brekhovskikh, *Waves in Layered Media*. Academic Press, New York, USA (1980).
 44. B. Maruyama, L. Shaw, M. Waterberry and D. Miracle, Automated deformation mapping in metal matrix composites, *Mater. Sci. Engng A*, **205**, 101–109 (1994).
 45. C. G. Rhodes and R. A. Spurling, Fiber–matrix reaction zone growth kinetics in SiC-reinforced Ti-6Al-4V as studied by transmission electron microscopy, in: *Recent Advances in Composites in the United States and Japan*, ASTM STP 864, J. R. Vinson and M. Taya (Eds), pp. 585–599. American Society for Testing and Materials, Philadelphia, USA (1985).
 46. C. G. Rhodes, A. K. Ghosh and R. A. Spurling, Ti-6Al-4V-2Ni as a matrix material for a SiC-reinforced composite, *Metall. Trans.* **18A**, 2151–2156 (1987).